IOP Publishing Nanotechnology

Nanotechnology 32 (2021) 265202 (10pp) https://doi.org/10.1088/1361-6528/abe78a

Tuning electrical and interfacial thermal properties of bilayer MoS_2 via electrochemical intercalation

Feng Xiong[1], Eilam Yalon[2,8], Connor J McClellan[2], Jinsong Zhang[3], Ozgur Burak Aslan[3,4,9], Aditya Sood[3,10], Jie Sun[3], Christopher M Andolina[5], Wissam A Saidi[5], Kenneth E Goodson[6], Tony F Heinz[4,7], Yi Cui[3,7] and Eric Pop[2,3]

[1] Department of Electrical and Computer Engineering, University of Pittsburgh, Pittsburgh, PA 15261, United States of America
[2] Department of Electrical Engineering, Stanford University, Stanford, CA 94305, United States of America
[3] Department of Materials Science and Engineering, Stanford University, Stanford, CA 94305, United States of America
[4] Department of Applied Physics, Stanford University, Stanford, CA 94305, United States of America
[5] Department of Mechanical Engineering and Materials Science, University of Pittsburgh, Pittsburgh, PA 15261, United States of America
[6] Department of Mechanical Engineering, Stanford University, Stanford, CA 94305, United States of America
[7] Stanford Institute for Materials and Energy Sciences, SLAC National Accelerator Laboratory, 2575 Sand Hill Road, Menlo Park, CA 94025, United States of America

E-mail: f.xiong@pitt.edu

Received 26 December 2020, revised 6 February 2021
Accepted for publication 18 February 2021
Published 6 April 2021

Abstract

Layered two-dimensional (2D) materials such as MoS_2 have attracted much attention for nano- and opto-electronics. Recently, intercalation (e.g. of ions, atoms, or molecules) has emerged as an effective technique to modulate material properties of such layered 2D films reversibly. We probe both the electrical and thermal properties of Li-intercalated bilayer MoS_2 nanosheets by combining electrical measurements and Raman spectroscopy. We demonstrate reversible modulation of carrier density over more than two orders of magnitude (from 0.8×10^{12} to 1.5×10^{14} cm^{-2}), and we simultaneously obtain the thermal boundary conductance between the bilayer and its supporting SiO_2 substrate for an intercalated system for the first time. This thermal coupling can be reversibly modulated by nearly a factor of eight, from 14 ± 4.0 MW m^{-2} K^{-1} before intercalation to 1.8 ± 0.9 MW m^{-2} K^{-1} when the MoS_2 is fully lithiated. These results reveal electrochemical intercalation as a reversible tool to modulate and control both electrical and thermal properties of 2D layers.

Supplementary material for this article is available online

Keywords: two-dimensional, intercalation, tunable, Raman, thermal, electrical

(Some figures may appear in colour only in the online journal)

1. Introduction

Two-dimensional (2D) materials such as molybdenum disulfide (MoS_2) are widely considered to be promising candidates for next-generation nanoelectronics due to their unique material

[8] Present Address: Department of Electrical Engineering, Technion 32000, Israel.
[9] Present Address: Department of Physics, Bogazici University, Istanbul 34342, Turkey.
[10] Present Address: Stanford Institute for Materials and Energy Sciences, SLAC National Accelerator Laboratory, 2575 Sand Hill Road, Menlo Park, CA 94025, United States of America.

properties (electrical, thermal, optical, mechanical) and their sub-nanometer thickness without dangling bonds [1, 2]. Potential applications for 2D materials include transistors [3, 4], interconnects [5], transparent electrodes [6], sensors [7], solar cells [8], thermoelectrics [9], and energy storage devices [10]. This wide range of applications has many requirements; thus, it is desirable to modulate the properties of 2D materials to optimize their performance for specific applications. Researchers have been actively developing ways to engineer electron and phonon transport in 2D materials via chemical doping, strain, and nanostructuring [11–13]. However, a controllable, reversible, and scalable method to engineer 2D material properties is still lacking. For instance, while some doping strategies effectively achieve high carrier concentrations [14, 15], it remains challenging to precisely control or modulate the doping level in 2D materials.

Intercalation has recently emerged as a promising technique to engineer 2D material properties for tunable electronic applications [16–20]. In layered 2D crystals, the van der Waals spacing between layers provides perfect sites to accommodate guest species such as ions and molecules (intercalants) through a process known as intercalation. These intercalants modify interlayer interactions in 2D thin films and affect material properties through charge transfer, band gap engineering, and phonon scattering [21–25]. Earlier efforts studying intercalation in 2D materials often employed a chemical intercalation approach [18, 26], where 2D crystals were immersed in a chemical solution containing the intended intercalant species (e.g. n-butyl lithium for chemical intercalation of lithium) for an extended time (up to 72 h). While chemical intercalation is relatively easy to perform and provides a convenient route to demonstrate its usefulness in doping and phase engineering 2D materials, this process is irreversible and lacks control over the intercalant concentration.

In contrast, in an electrochemical intercalation process, the number of ions (e.g. Li^+) intercalated between the 2D layers can be precisely and reversibly modulated by controlling the number of electrical charges (charging current $\times$ time) transferred to the host materials [16, 17, 27, 28]. While electrochemical intercalation is extensively studied and forms the backbone of Li ion battery (LIB) industry, there has been limited work done leveraging this technique to engineer fundamental material properties in 2D materials. Electrically, electrochemical Li intercalation has demonstrated tunable electrical conductance over 2–3 orders of magnitude in graphitic thin films [17], few-layer MoS_2 [16], as well as 2D heterostructures [29]. Thermally, Li intercalation has been employed to achieve ~8–10 $\times$ modulation of cross-plane thermal conductance (combined volumetric contribution of MoS_2, and interfacial contributions of Al/MoS_2 and MoS_2/SiO_2) in MoS_2 thin films [30] (~10 nm thick) and up to 5$\times$ change in cross-plane thermal conductivity in bulk MoS_2 samples [21] (~10–20 μm thick). However, while these earlier studies provided valuable insights on how intercalation affects electrical and thermal transport in 2D materials, detailed studies on the charge transfer process in intercalated 2D films and the effect of intercalants on thermal boundary conductance (TBC) between 2D films and the substrate, a key parameter in determining energy dissipation in 2D electronics [31–33], are still lacking. The TBC plays an important role in thermal transport across sub-100 nm thin films, even when quasi-ballistic effects are considered [34].

In this work, we investigate how the carrier concentration in MoS_2 and the TBC at MoS_2/SiO_2 interface vary as a function of Li concentration through electrical Hall measurements and Raman spectroscopy. In addition, prior intercalation studies often employ the well-characterized liquid electrolyte and Li metal as the reference electrode [16, 17], which are highly reactive and flammable and may not be ideal for electronics applications. We report a solid-state electrochemical intercalation platform using $LiClO_4$ in polyethylene oxide (PEO) as a solid electrolyte and the air-stable $LiFePO_4$ (LFP) as the reference electrode (Li reservoir). Our work addresses reversible doping and thermal dissipation that are two fundamental issues in 2D electronics, and provides a promising path towards tunable 2D electronics.

2. Experiments

2.1. Device fabrication

MoS_2 flakes were mechanically exfoliated onto a highly doped (p-type) Si substrate with 90 nm thick thermally grown SiO_2. The bilayer MoS_2 flakes were pre-sorted with an optical microscope and later confirmed with Raman spectroscopy and atomic force microscopy (AFM). The MoS_2 flakes were patterned into Hall structures with e-beam lithography and XeF_2 etching. Electrode contacts (Ti/Au, 1/50 nm) were deposited with e-beam evaporation.

2.2. Intercalation

Our 2D electrochemical device is similar to a planar nano-battery with MoS_2 and lithium iron phosphate $LiFePO_4$ serving as the working and reference/counter electrodes, respectively. The solid electrolyte was prepared by dissolving $LiClO_4$ (Sigma Aldrich) into PEO (Sigma Aldrich) matrix. PEO and $LiClO_4$ powders (500 and 150 mg, respectively) were mixed with 7.5 ml of anhydrous methanol and stirred for 12 h at 50 °C. An electrochemical workstation (Biologic SP-150) was used to perform the Li intercalation and de-intercalation and measure MoS_2 electrochemical potential.

2.3. Characterization and measurements

Raman spectroscopy was performed with a Horiba LabRam instrument with a 532 nm green laser and 1800 mm^{-1} grating. A 100$\times$ long working distance objective (N.A. = 0.6) was used to accommodate the MoS_2 electrochemical devices with PEO electrolyte. For Raman thermometry measurements, the temperature calibrations were carried out with a Linkam THMS600 stage. Part of the electrical transport measurements was carried out using a semiconductor parameter analyzer (Keithley 4200 SCS). The temperature-dependent Hall measurement was conducted in a Quantum Design PPMS-7 system with digital lock-in amplifiers (Stanford Research Systems SR830).

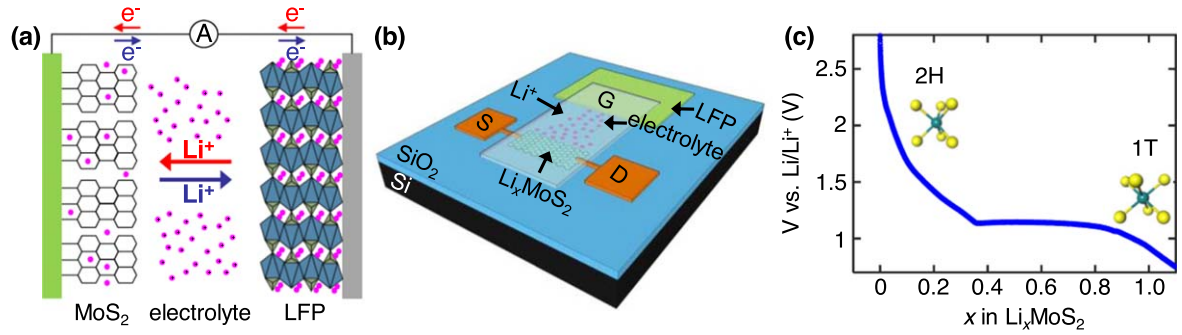

Figure 1. Electrochemical intercalation. (a) Schematics of electrochemical intercalation process with MoS_2 sheets as the working electrode and $LiFePO_4$ (LFP) as the reference electrode. The solid electrolyte is $LiClO_4$ in PEO. The red and blue arrows represent the direction of Li ions (in electrolyte) and electrons (in external circuit) movements during intercalation and de-intercalation, respectively. (b) Schematics of electrochemical intercalation device. (c) Galvanostatic discharge curve of MoS_2 with respect to LFP. The electrochemical potential (*y*-axis) is normalized to Li/Li^+ potential by adding 3.5 V, the potential of LFP with respect to Li/Li^+. The 2H to 1T phase transition plateau for MoS_2 occurs at 1.1 V with respect to Li, similar to previous reports [16, 35, 36]. This indicates that LFP works well as an air-stable reference electrode to replace the highly reactive Li metal.

3. Results and discussion

3.1. Electrochemical intercalation

Figure 1 shows the schematics of the electrochemical intercalation process, where Li ions move in and out of the interlayer spacing in 2D materials, depending on the external electrical current flow. Our intercalation platform consists of the 2D material (the working electrode), a Li reservoir (the reference electrode), and the electrolyte to allow ionic movement (no electron transport). The main advantage of electrochemical intercalation over the chemical intercalation process is that we can achieve reversible control over the intercalant concentration [16]. Governed by charge neutrality, for every negatively charged electron that flows from the reference electrode to the working electrode during intercalation, a positively charged Li^+ ion moves from the reference electrode to the working electrode, i.e. a Li^+ ion is intercalated in the 2D material. Thus, we can precisely modulate the Li concentration in the host 2D material by controlling the total amount of charge transferred from the reference electrode to the 2D material (current × time). To increase the Li content in 2D materials, i.e. intercalation, we will flow electrons from the reference electrode to the 2D material via an external circuit (indicated by the direction of red arrows in figure 1(a)); to decrease the Li content, i.e. de-intercalation, we will need to reverse the current flow (blue arrows in figure 1(a)). This allows us to engineer the electrical and thermal properties of our device by controlling the Li concentration in 2D materials.

We adopt the air-stable $LiFePO_4$ (LFP) (instead of the highly reactive Li metal) as the reference electrode (figure 1(b)) in our device. LFP has a very stable electrochemical plateau (~3.4 V versus Li/Li^+) when its lithiation content is between 10% and 90% [37, 38]. LFP also has a long lifetime and a high power density; therefore, it has been used as a cathode material in rechargeable LIB [37, 38]. We also utilize a solid electrolyte, $LiClO_4$, in PEO for this work, instead of the liquid electrolyte ($LiPF_6$ in EC/DEC solution) that is prevalent in LIBs. Even though a liquid electrolyte typically has better ionic mobility than the polymer electrolyte, it is prone to low-charge retention, leakage issues, and thermal instability at low and high operating temperatures [39]. This would severely limit the application of intercalation in tunable electronics. In contrast, the PEO electrolyte has better chemical and thermal stability, comparable ionic mobility, and higher energy density [40].

In principle, we could calculate the exact Li content in our 2D films, knowing the current flow and exact amount of charge flowing into the 2D nanosheet, as well as the exact molecular mass of the host 2D material. However, it is impractical to measure the weight of our MoS_2 nanosheet accurately. Thus, we first performed a galvanostatic discharge measurement (figure 1(c)) on bulk MoS_2 powder as a calibration, where we can measure the weight of the bulk MoS_2 accurately. Since the galvanostatic discharge measurement only depends on the chemical composition of the material, we expect the calibration result of the bulk powder to be transferrable to MoS_2 thin films. From our calibration, we established a correlation between the electrochemical potential with respect to Li/Li^+ and Li concentration in intercalated Li_xMoS_2 (figure 1(c)). The plateau at 1.1 V represents the 2H to 1T phase transition in MoS_2, consistent with previously reported values [16, 35, 36]. With the calibration result, we can modulate the Li content in MoS_2 conveniently by varying the electrochemical potential of MoS_2 with respect to Li/Li^+ and read the Li concentration by comparing the potential in our calibrated sample. To prevent the irreversible conversion reaction that forms Li_2S [35], we avoid lithiating MoS_2 below 0.9 V with respect to Li/Li^+ in this work.

3.2. Electrical transport

We fabricated Hall bar structures on bilayer MoS_2 samples to investigate how much carrier modulation we can achieve with electrochemical intercalation. The schematics and optical image of our electrochemical devices are shown in figure 2(a). Figure 2(a) inset shows the MoS_2 thickness (t_{MoS2}) to be ~1.7 nm (bilayer) through AFM. More fabrication details can be found in the Methods and supporting information

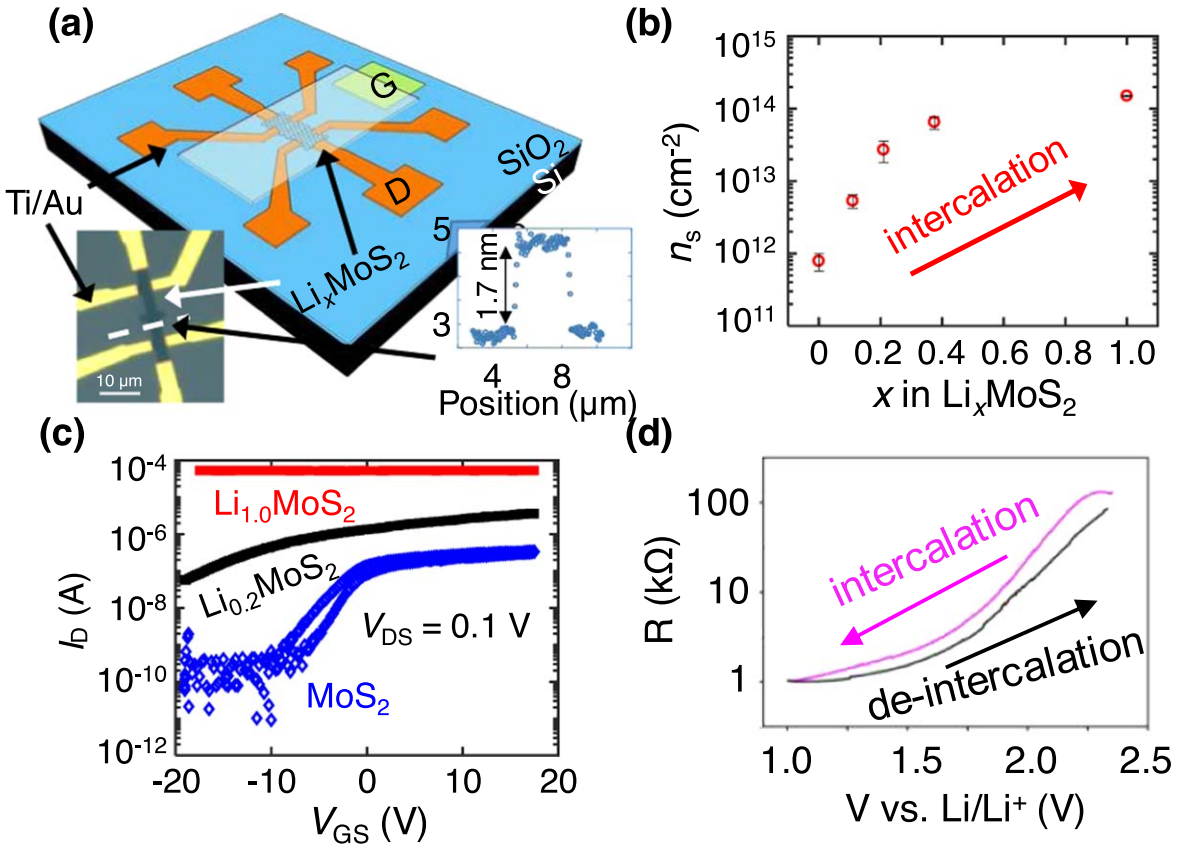

Figure 2. Tuning MoS_2 carrier concentration via intercalation. (a) Schematics of Hall bar structure with electrochemical intercalation platform. Inset is an optical image of fabricated MoS_2 device with Hall bar structure. The inset shows the AFM measurement of the MoS_2 device, confirming bilayer thickness (~1.7 nm). (b) Carrier concentration in MoS_2 as a function of Li concentration, controlled by the potential difference of MoS_2 with respect to the reference electrode. (c) Transfer characteristics of pristine MoS_2 (blue), $Li_{0.2}MoS_2$ (black), $Li_{1.0}MoS_2$ (red). The channel conductance increases as carrier concentration increases due to Li intercalation. $Li_{1.0}MoS_2$ shows metallic behavior (no V_{GS} dependence) because it is in the 1T phase. (d) Reversible electrical properties as we lithiate and de-lithiate the MoS_2 thin film (a different bilayer sample than the one depicted in (a)–(c)) via changing its electrochemical potential.

sections (available online at stacks.iop.org/NANO/32/265202/mmedia).

Next, we applied the polymer electrolyte ($LiClO_4$ in PEO) to cover the entire MoS_2 channel and the reference electrode (LFP, see Methods for more details). This electrically-insulating solid polymer allows ionic exchange between LFP and the 2D material. Unlike an electric-double-layer transistor (EDLT), which does not have a reference electrode (only a metal contact) [41–44], we can controllably perform electrochemical intercalation in our device with a well-defined electrochemical reference potential (figure 1(a)). This provides additional control in electronics applications because the effect from electrochemical intercalation is long-term, while the ionic gating effect in EDLT is short-term (only persist with applied gate voltage). As we monitor the electrochemical potential of MoS_2 with respect to the reference electrode, we can precisely and reversibly tune the Li concentration in MoS_2 by adjusting the potential between MoS_2 and the reference electrode (figure 1(c)).

By controlling the electrochemical potential of MoS_2 with respect to our reference LFP electrode, we can intercalate/de-intercalate Li ions and therefore modulate the carrier concentrations in MoS_2, similar to a charging/discharging process in a LIB. Initially, the pristine MoS_2 had an electrochemical potential of 2.5 V versus Li/Li^+, i.e. −0.95 V with respect to LFP, since partially lithiated LFP has a stable potential plateau of 3.45 with respect to Li/Li^+ (see Methods for more details) [37, 38]. The 2D carrier concentration n_s in this MoS_2 flake was 8×10^{11} cm^{-2} before Li intercalation, as extracted from Hall measurement. As we intercalate more Li ions into MoS_2 by lowering the potential of MoS_2 with respect to the reference electrode (figure 1(c)), we observe a significant increase in carrier concentration (figure 2(b)), with n_s reaching 1.5×10^{14} cm^{-2} when Li concentration approached the maximum intercalation capacity $Li_{1.0}MoS_2$, equivalent to one Li ion per unit cell. This large increase in carrier concentration is likely due to the combined results of charge transfer from the intercalated Li ions and the effect of ionic gating. We also measured the temperature dependence of the lithiated MoS_2 device's electrical resistance from room temperature down to 2 K (see figure S2 in the supporting information) but did not observe any superconductive behavior in our device.

The Hall bar structure also behaves as a 2D transistor with a Si back gate below the 90 nm thick SiO_2. Figure 2(c) shows the transfer curves of a typical device at room temperature with different Li concentrations under a source-drain

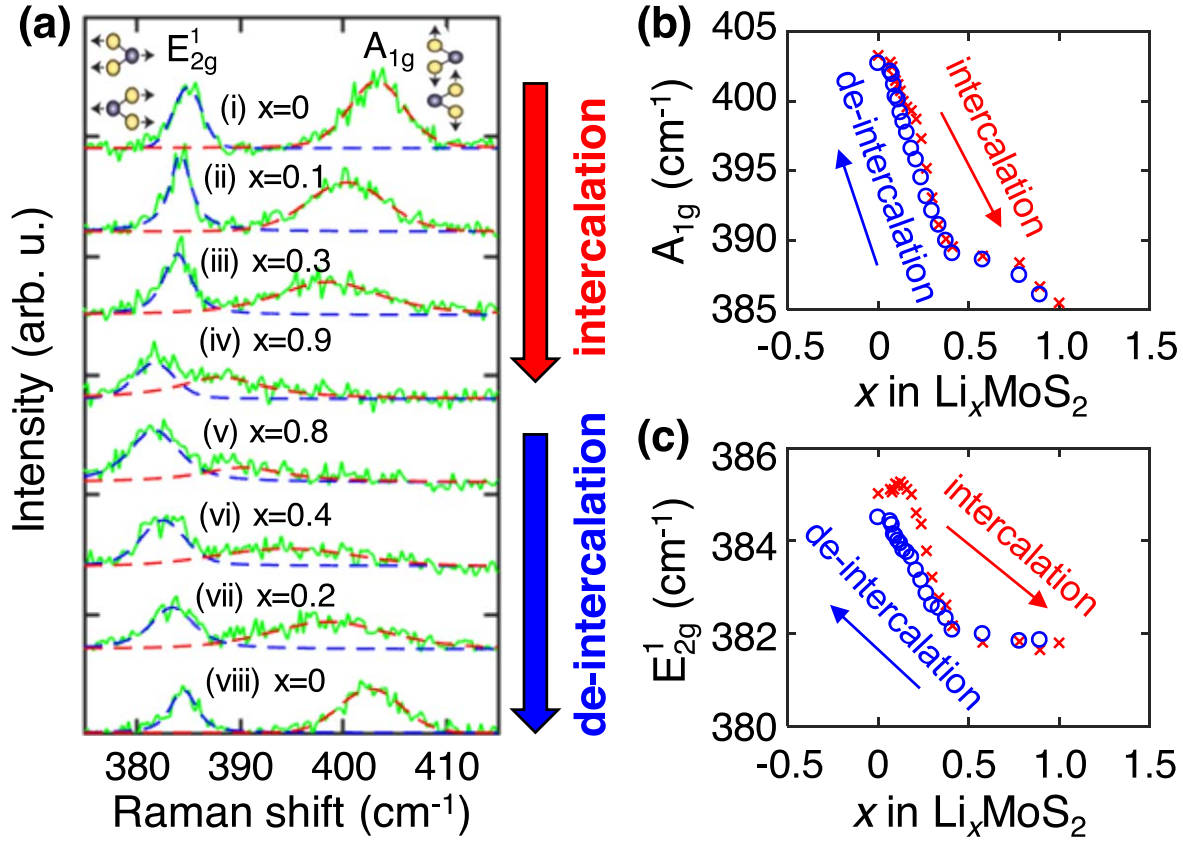

Figure 3. Raman spectroscopy of Li-intercalated MoS_2. (a) Raman spectroscopy of bilayer MoS_2 thin film during the intercalation (i)–(iv) and de-intercalation (v)–(viii) steps. Green curves are the raw data; blue and red curves are the fitted results for the Raman modes, E^1_{2g} and A_{1g}, respectively. The insets show the corresponding vibrational modes. (b)–(c) The measured frequency shift of A_{1g} and E^1_{2g} modes as a function of Li content in Li_xMoS_2. Red crosses and blue circles represent the intercalation and the subsequent de-intercalation steps, respectively.

bias $V_{DS} = 0.1$ V. Before Li intercalation, the exfoliated MoS_2 (blue curve in figure 2(c)) was in a semiconducting 2H phase and showed an on/off ratio of ~1000× through back-gate control. Upon Li intercalation (black curve, $Li_{0.2}MoS_2$), we noticed an increase in channel conductance due to doping and decreased on/off ratio (~50×). When the MoS_2 flake was fully lithiated to $Li_{1.0}MoS_2$ (red curve), the channel became metallic as MoS_2 underwent a 2H (semiconducting) to 1T (metallic) phase transformation upon lithiation as previously reported [16, 18, 35, 36]. We observed ~500× improvement in drive current I_{on} upon Li intercalation ($Li_{1.0}MoS_2$) likely because of the higher carrier concentration [29] (~200×) upon intercalation as well as lower contact resistance due to the semiconducting-to-metallic phase transition [18, 45]. This 2H to 1T phase transition is likely triggered by the strain from the influx of Li ions [46]. Upon intercalation, Li atoms occupy octahedral sites between the 2H-MoS_2 layers, forming an unstable 2H-Li_xMoS_2 phase. As more Li atoms enter the MoS_2 structure [47], the strain causes the crystal structure to transform into the thermodynamically-stable 1T-Li_xMoS_2 phase with stacking sequence AA shown in the figure 1(c) inset. The associated (~2%–5%) increase in interlayer spacing allows it to accommodate more Li atoms in the unit cell, as similarly reported in previous *in situ* XRD measurements [23] and first-principle calculations [46]. The change in electrical conductance is reversible as we lithiate and de-lithiate the MoS_2 device (figure 2(d)), opening up opportunities for applications in memory and synaptic devices[48–51].

3.3. Raman spectroscopy

We also studied how intercalation affected the doping and strain in these 2D layers via Raman microscopy. Figure 3 illustrates our Raman measurements on a bilayer MoS_2 flake as we intercalate and de-intercalate the device. Green curves are the original Raman spectra; blue and red curves represent the fitted E^1_{2g} and A_{1g} modes, respectively. By intercalating Li^+ ions into a bilayer MoS_2 film (series (i)–(iv) in figure 3(a)), we noticed a significant peak shift and broadening of the A_{1g} mode (figure 3(b)), which is attributed to doping in MoS_2 [16, 52, 53]. Similarly, the E^1_{2g} mode also decreased in frequency (figure 3(c)) and broadened upon intercalation, albeit to a much lesser extent. This likely indicates strain build-up in the lattice due to the influx of Li^+ ions [16, 54]. These changes in Raman spectra were fully reversible as we moved Li^+ ions out of MoS_2 during the de-intercalation process [series (v)–(viii) in figure 3(a)] and are consistent with our density functional theory calculations (see figure S7 in the supporting information). The A_{1g} mode shift

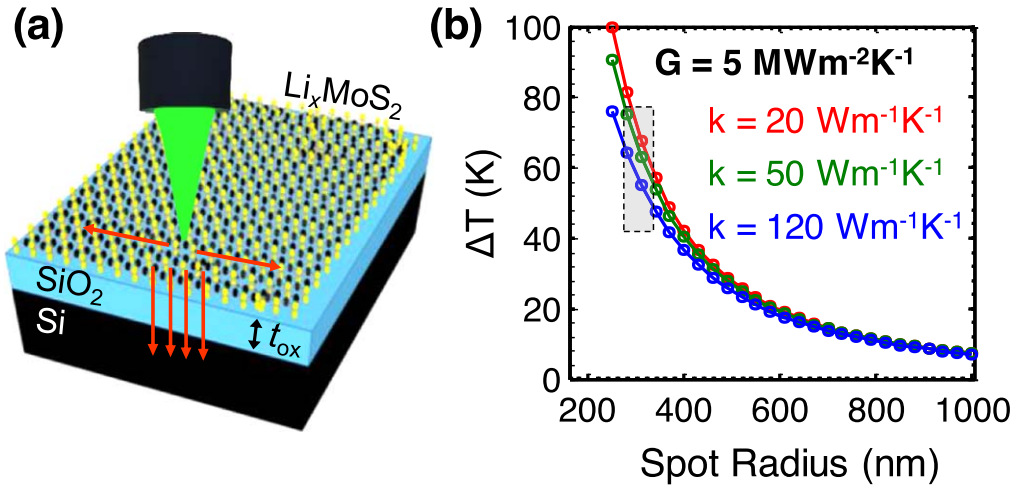

Figure 4. MoS_2/SiO_2 thermal boundary conductance (TBC) before and after intercalation. (a) Schematic of Raman thermometry platform of the bilayer MoS_2 on the SiO_2/Si substrate. (b) The simulated temperature rise of MoS_2 as a function of laser spot size at an absorbed power of 1.2 mW, when the MoS_2/SiO_2 TBC $= 5$ MW m^{-2} K^{-1}, near the lower bound of the TBC after intercalation. Red, green and blue curves are for in-plane thermal conductivity of MoS_2 $k = 20$, 50, and 120 W m^{-1} K^{-1}, respectively. This suggests that the temperature rise in MoS_2 is insensitive to its in-plane k, most of the heat flows through the SiO_2/Si substrate, and we can fit the TBC of MoS_2/SiO_2 by assuming a typical $k \approx 50$ W m^{-1} K^{-1}.

was as large as 18 cm^{-1} at $Li_{1.0}MoS_2$ (figure 3(b)), confirming a heavy doping concentration ($n_s = 1.5 \times 10^{14}$ cm^{-2} from our Hall measurement in figure 2(c)) [25].

3.4. Raman thermometry

In addition to the use of Raman spectroscopy to probe the carrier concentration of intercalated Li_xMoS_2, we also employ a Raman thermometry technique (figure 4(a)) to characterize how the TBC between bilayer MoS_2 and its supporting substrate (SiO_2/Si) changes as we intercalate and de-intercalate Li ions into the van der Waals gap between MoS_2 layers and between the bottom MoS_2 layer and the SiO_2 substrate. As illustrated in figure 4(a), TBCs between 2D thin films and their supporting substrate play significant roles in limiting the heat and energy dissipation of 2D devices [31–33, 55, 56]. Drive currents in 2D transistors are limited by their local temperatures, which TBCs largely determine [57]. However, measuring the TBC in ultrathin 2D electronics has been challenging due to uncertainties in measuring the heat flow and the local temperature [58, 59].

Recently, we reported the TBC of pristine monolayer MoS_2 on SiO_2 via Raman thermometry [31, 33]. In a Raman thermometry measurement, we characterize the temperature rise of 2D thin films optically (through peak shift of the Raman mode) as a function of the input power (either optically from the Raman laser or electrically by Joule heating). We then fit the temperature rise and the input power into a thermal model [60] to calculate the TBC and the in-plane thermal conductivity of the 2D film by solving the heat diffusion equation in our model [33].

For bilayer MoS_2 thin films on SiO_2/Si substrates and with a spot size r_o between 310 and 370 nm (without and with electrolyte through a 100× objective, see figure S3 in the supporting information for more details), we expect most of the heat in MoS_2 will be dissipated through the substrate and rendering the system to be insensitive to the in-plane thermal conductivity of MoS_2, as shown in figure 4(b) (see figure S4 in the supporting information for more analysis). This allows us to only use a supported structure (figure 4(a)) to calculate our single fitting parameter, the TBC at the MoS_2/SiO_2 interface significantly simplifies our measurement and analysis.

A key parameter in Raman thermometry is the power absorbed (P_{abs}) by bilayer MoS_2. A significant portion of the uncertainty in optically-heated Raman thermometry measurements stems from P_{abs} estimations because it is challenging to directly measure the absorbed power of a 2D thin film supported on a substrate where multiple optical reflections interfere. We employed the following approach to minimize those uncertainties. The power absorbed by such a 2D film is calculated as follows: $P_{abs} = P_{in}\alpha_f E$, where P_{in} is the incident laser power, α_f is the absorption coefficient of free-standing MoS_2. E is a wavelength-dependent enhancement factor, the intensity of the electric field (of the electromagnetic wave of the laser) at the top surface of SiO_2/Si substrate relative to the intensity of the incident electric field, accounting for the multiple reflections within the SiO_2/Si substrate. We characterized the incident laser power and the spot radius r_o during our calibration measurements (see figure S3 in the supporting information for more details).

We measured the absorption coefficient of free-standing monolayer MoS_2 over a range of temperatures (see figure S6 in the supporting information). This temperature-dependence of α_f is important as we observed a 30% increase in absorption (at a laser wavelength of 532 nm) at 250 °C compared to that at room temperature. Neglecting this temperature dependence (and therefore underestimating P_{abs}) will underestimate the TBC in the Raman thermometry analysis. We expect the optical dielectric functions of monolayer and bilayer MoS_2 to be very similar away from the peak energies of those transitions, such as at a wavelength of 532 nm. Thus we assume that the absorption of free-standing

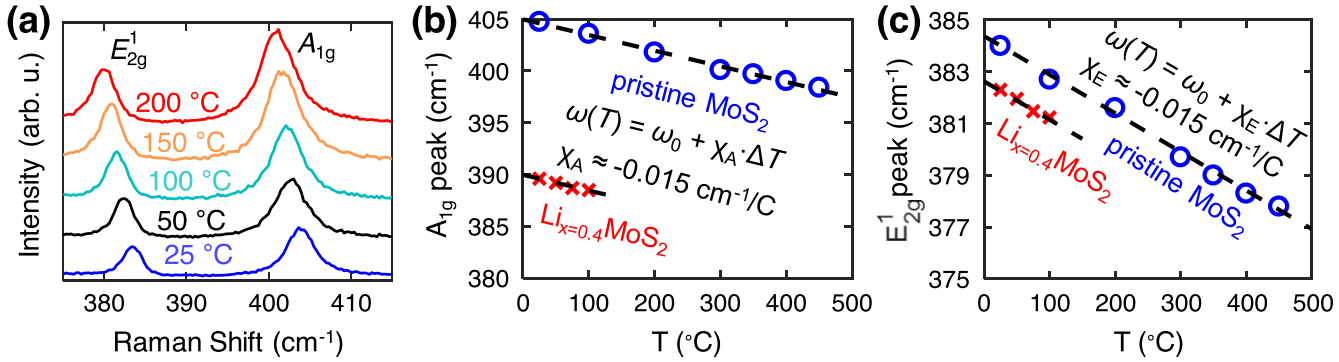

Figure 5. Temperature dependence of Raman peaks. (a) Raman spectra of pristine bilayer MoS_2 as a function of temperature. (b)–(c) Temperature calibration by substrate heating for A_{1g} and E^1_{2g} modes, respectively. Blue and red circles represent calibration for pristine MoS_2 and intercalated $Li_{0.4}MoS_2$, respectively. The slopes of the linear fits are the temperature coefficients χ_A and χ_E for A_{1g} and E^1_{2g} modes, respectively.

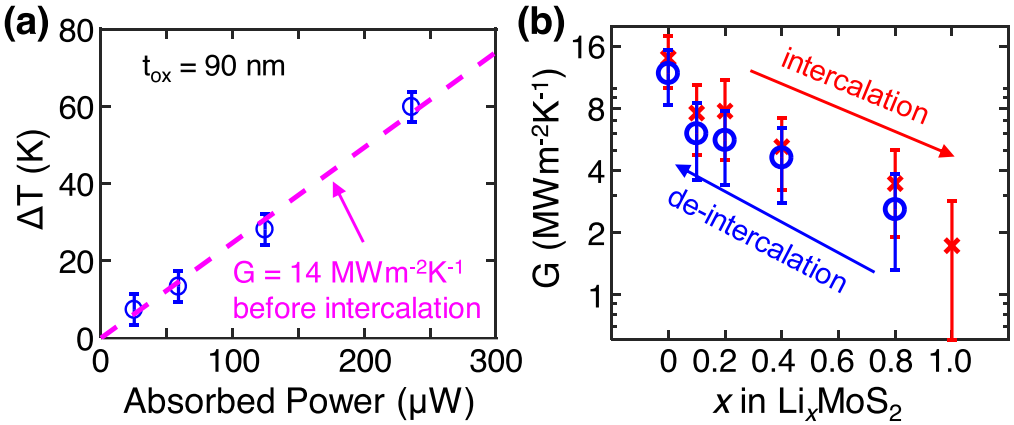

Figure 6. Thermal boundary conductance (TBC) between MoS_2 and SiO_2. (a) The measured temperature rise of a pristine bilayer MoS_2 device (no intercalation) versus absorbed laser power. The dashed line represents a thermal resistance with TBC = 14 ± 4 MW m^{-2} K^{-1}. (b) TBC as a function of Li concentration in MoS_2. As we intercalate (red crosses) more Li ions into MoS_2, the TBC decreases to ~1.8 MW m^{-2} K^{-1} at $Li_{1.0}MoS_2$. As we de-intercalate (blue circles) Li ions out of the system, the TBC almost recovers to its original value (~11.8 MW m^{-2} K^{-1}).

bilayer MoS_2 at 532 nm to be twice that of the monolayer MoS_2 at 14% at 300 K, with similar temperature dependence as monolayer MoS_2 (see more discussion in supporting information section S6) [33]. We measured the absorption coefficient of lithiated MoS_2 in an earlier study [16], where we observed a 60% decrease in absorption (8.4% for bilayer $Li_{1.0}MoS_2$) at 532 nm due to the 2H to 1T phase transformation and the associated elimination of a band gap (see figure S6 in the supporting information). We also calculated the enhancement factor (~1.46 at 532 nm) based on the thickness, interface, and refractive index of the materials in our stack (PEO/MoS_2/SiO_2/Si). More details on the estimation of the absorbed power can be found in the supporting information section S6 and our prior analysis [33].

Another important parameter in Raman thermometry is the temperature rise $\Delta T = T - T_0$, where T and $T_0 = 300$ K are the sample and background temperature, respectively. As shown in figure 5(a), we first performed the temperature calibrations using a Linkam heating stage to measure the Raman peak position (A_{1g} and E^1_{2g} modes for MoS_2) as a function of the sample temperature (through stage heating). This allows us to fit a linear relationship between the Raman peak position ω and the sample temperature T: $\omega(T) = \omega_0 + \chi(T - T_0)$, where ω_0 is the peak position at room temperature T_0 and χ is the temperature dependence coefficient for the particular Raman mode. For E^1_{2g} and A_{1g} modes in pristine bilayer MoS_2, χ_E, and χ_A were fitted to be -0.015 ± 0.002 cm^{-1} °C^{-1} and -0.015 ± 0.002 cm^{-1} °C^{-1}, as shown in the blue dashed lines in figures 5(b) and (c).

For intercalated Li_xMoS_2, the initial peak position and temperature dependence coefficient can differ from that of pristine MoS_2, as illustrated in figure 3. Thus, we performed a series of temperature calibrations at different Li concentrations, $x = 0$, 0.2, 0.4, 0.8, and 1.0, for our Li_xMoS_2 samples. The calibration and fitted results for $Li_{0.4}MoS_2$ are shown in figures 5(b) and (c), where the temperature dependence coefficients are found to be similar for Li_xMoS_2 samples (more details on the calibrations can be found in figure S5 in the supporting information). We kept the laser power low (and therefore Li_xMoS_2 temperature <100 °C) during our calibration and actual thermometry measurements to avoid unintentional phase transformation and minimize ionic diffusion (and therefore a change in carrier concentration) that has been observed in high-temperature annealing (>300 °C) of chemically lithiated MoS_2 thin films [18, 61].

As shown in figure 6(a), the TBC at the bilayer MoS_2/SiO_2 interface before intercalation is $G = 14 \pm 4.0$ MW m^{-2} K^{-1},

consistent with previous reports (~15 MW m^{-2} K^{-1}) for monolayer MoS_2 with electrical [31] and optical [33] heating. Upon Li intercalation (figure 6(b)), we observe a significant decrease in TBC at the MoS_2/SiO_2 interface, to $G = 1.8 \pm 0.9$ MW m^{-2} K^{-1} for $Li_{1.0}MoS_2$. This large decrease in TBC is likely due to a combination of effects, including an increase in the van der Waals spacing at the MoS_2/SiO_2 interface and changes in MoS_2/SiO_2 bonding. Upon de-intercalation, the TBC can be mostly recovered to its pre-lithiation value when we removed Li ions from the system ($G = 11.8 \pm 3.5$ MW m^{-2} K^{-1}). This large and reversible TBC modulation opens interesting opportunities to engineer the heat dissipation for 2D applications such as nanoscale thermal transistors [30] and thermoelectric devices.

4. Conclusion

In summary, we developed a solid-state Li intercalation platform for 2D materials and achieved reversible control of their electrical and thermal properties via electrochemical intercalation. Through Hall measurements, we demonstrated ~200× tuning of carrier concentration in Li-intercalated bilayer MoS_2, ranging from 0.8×10^{12} to 1.5×10^{14} cm^{-2}. Combining with an improved contact resistance, almost three orders of magnitude increase (500×) in the drive current of such bilayer MoS_2 transistors. Raman spectroscopy confirmed the reversible doping effect, recording peak shifts as large as 18 cm^{-1} and 3 cm^{-1} for A_{1g} and E^1_{2g} modes of MoS_2, respectively. Using Raman thermometry, we extracted the TBC between MoS_2 and SiO_2 to be 14 ± 4.0 MW m^{-2} K^{-1} before intercalation, and as low as 1.8 ± 0.9 MW m^{-2} K^{-1} after intercalation, due to weakened bonding and phonon scattering. Thus our study suggests that electrochemical intercalation is a powerful technique to engineer and reversibly tune 2D material electrical and thermal properties. Our findings also provide a convenient method to measure the carrier concentration and TBC of 2D materials using Raman spectroscopy, crucial for 2D electronic applications.

Acknowledgments

This work was supported in part by National Science Foundation (NSF) EFRI 2-DARE grant 1542883, by the Air Force Office of Scientific Research grant FA9550-14-1-0251, by the NSF Center for Power Optimization of Electro-Thermal Systems (POETS) under grant EEC-1449548. FX acknowledges partial support by the NSF ECCS grant 1901864. EY acknowledges partial support from Ilan Ramon Fulbright Fellowship and from the Andrew and Erna Finci Viterbi Foundation. WAS acknowledges financial support from the National Science Foundation (Award No. DMR-1809085). YC acknowledges the support by the Department of Energy (DOE), Office of Basic Energy Sciences, Division of Materials Sciences and Engineering (contract no. DE-AC02-76SF00515). We are grateful for computing time provided by the CRC resources at the University of Pittsburgh. YC, TH, and OBA acknowledge support by the Department of Energy (DOE), Office of Basic Energy Sciences, Division of Materials Sciences and Engineering (contract no. DE-AC02-76SF00515.

Data availability statement

The data that support the findings of this study are available upon reasonable request from the authors.

ORCID iDs

Feng Xiong https://orcid.org/0000-0001-8383-5182
Eilam Yalon https://orcid.org/0000-0001-7965-459X
Connor J McClellan https://orcid.org/0000-0002-8733-9968
Ozgur Burak Aslan https://orcid.org/0000-0002-0925-3026
Aditya Sood https://orcid.org/0000-0002-4319-666X
Christopher M Andolina https://orcid.org/0000-0003-2157-9114
Wissam A Saidi https://orcid.org/0000-0001-6714-4832
Tony F Heinz https://orcid.org/0000-0003-1365-9464
Yi Cui https://orcid.org/0000-0002-6103-6352
Eric Pop https://orcid.org/0000-0003-0436-8534

References

[1] Duan X D, Wang C, Pan A L, Yu R Q and Duan X F 2015 Two-dimensional transition metal dichalcogenides as atomically thin semiconductors: opportunities and challenges *Chem. Soc. Rev.* **44** 8859–76
[2] Mak K F and Shan J 2016 Photonics and optoelectronics of 2D semiconductor transition metal dichalcogenides *Nat. Photon.* **10** 216–26
[3] Radisavljevic B, Whitwick M B and Kis A 2011 Integrated circuits and logic operations based on single-layer MoS_2 *ACS Nano* **5** 9934–8
[4] Alam M H, Xu Z, Chowdhury S, Jiang Z, Taneja D, Banerjee S K, Lai K, Braga M H and Akinwande D 2020 Lithium-ion electrolytic substrates for sub-1V high-performance transition metal dichalcogenide transistors and amplifiers *Nat. Commun.* **11** 3203
[5] Mleczko M J, Xu R L, Okabe K, Kuo H-H, Fisher I R, Wong H S P, Nishi Y and Pop E 2016 High current density and low thermal conductivity of atomically thin semimetallic WTe_2 *ACS Nano* **10** 7507–14
[6] Kim C-L, Jung C-W, Oh Y-J and Kim D-E 2017 A highly flexible transparent conductive electrode based on nanomaterials *NPG Asia Mater.* **9** 438
[7] Shim J, Banerjee S, Qiu H, Smithe K K H, Estrada D, Bello J, Pop E, Schulten K and Bashir R 2017 Detection of methylation on dsDNA using nanopores in a MoS_2 membrane *Nanoscale* **9** 14836–45
[8] Wi S, Kim H, Chen M K, Nam H, Guo L J, Meyhofer E and Liang X G 2014 Enhancement of photovoltaic response in multilayer MoS_2 induced by plasma doping *ACS Nano* **8** 5270–81
[9] Huang Z W, Wu T M, Kong S, Meng Q L, Zhuang W, Jiang P and Bao X H 2016 Enhancement of anisotropic thermoelectric performance of tungsten disulfide by titanium doping *J. Mater. Chem.* A **4** 10159–65

[10] Zhou J W, Qin J, Zhang X, Shi C S, Liu E Z, Li J J, Zhao N Q and He C N 2015 2D space-confined synthesis of few-layer MoS_2 anchored on carbon nanosheet for lithium-ion battery anode *ACS Nano* **9** 3837–48

[11] Conley H J, Wang B, Ziegler J I, Haglund R F, Pantelides S T and Bolotin K I 2013 Bandgap engineering of strained monolayer and bilayer MoS_2 *Nano Lett.* **13** 3626–30

[12] Yang L M *et al* 2014 Chloride molecular doping technique on 2D materials: WS_2 and MoS_2 *Nano Lett.* **14** 6275–80

[13] Novoselov K S, Mishchenko A, Carvalho A and Neto A H C 2016 2D materials and van der Waals heterostructures *Science* **353** 461–6

[14] Fang H, Tosun M, Seol G, Chang T C, Takei K, Guo J and Javey A 2013 Degenerate n-doping of few-layer transition metal dichalcogenides by potassium *Nano Lett.* **13** 1991–5

[15] Huang C, Jin Y B, Wang W Y, Tang L, Song C Y and Xiu F X 2017 Manganese and chromium doping in atomically thin MoS_2 *J. Semicond.* **38** 033004

[16] Xiong F, Wang H T, Liu X G, Sun J, Brongersma M, Pop E and Cui Y 2015 Li intercalation in MoS_2: *in situ* observation of its dynamics and tuning optical and electrical properties *Nano Lett.* **15** 6777–84

[17] Bao W Z *et al* 2014 Approaching the limits of transparency and conductivity in graphitic materials through lithium intercalation *Nat. Commun.* **5** 4224

[18] Kappera R, Voiry D, Yalcin S E, Branch B, Gupta G, Mohite A D and Chhowalla M 2014 Phase-engineered low-resistance contacts for ultrathin MoS_2 transistors *Nat. Mater.* **13** 1128–34

[19] Wan J, Lacey S D, Dai J, Bao W, Fuhrer M S and Hu L 2016 Tuning two-dimensional nanomaterials by intercalation: materials, properties and applications *Chem. Soc. Rev.* **45** 6742–65

[20] Stark M S, Kuntz K L, Martens S J and Warren S C 2019 Intercalation of layered materials from bulk to 2D *Adv. Mater.* **31** 1808213

[21] Zhu G, Liu J, Zheng Q, Zhang R, Li D, Banerjee D and Cahill D G 2016 Tuning thermal conductivity in molybdenum disulfide by electrochemical intercalation *Nat. Commun.* **7** 13211

[22] Kang J S, Ke M and Hu Y 2017 Ionic intercalation in two-dimensional van der Waals materials: *in situ* characterization and electrochemical control of the anisotropic thermal conductivity of black phosphorus *Nano Lett.* **17** 1431–8

[23] Ng H K *et al* 2019 Effects of structural phase transition on thermoelectric performance in lithium-intercalated molybdenum disulfide ($LixMoS_2$) *ACS Appl. Mater. Interfaces* **11** 12184–9

[24] Gong Y *et al* 2018 Spatially controlled doping of two-dimensional SnS_2 through intercalation for electronics *Nat. Nanotechnol.* **13** 294–9

[25] Zhang J *et al* 2018 Reversible and selective ion intercalation through the top surface of few-layer MoS_2 *Nat. Commun.* **9** 5289

[26] Holgate T C, Liu Y F, Hitchcock D, Tritt T M and He J 2013 Thermoelectric properties of Li-intercalated $ZrSe_2$ single crystals *J. Electron. Mater.* **42** 1751–5

[27] Kühne M, Paolucci F, Popovic J, Ostrovsky P M, Maier J and Smet J H 2017 Ultrafast lithium diffusion in bilayer graphene *Nat. Nanotechnol.* **12** 895–900

[28] Kühne M, Börrnert F, Fecher S, Ghorbani-Asl M, Biskupek J, Samuelis D, Krasheninnikov A V, Kaiser U and Smet J H 2018 Reversible superdense ordering of lithium between two graphene sheets *Nature* **564** 234–9

[29] Bediako D K, Rezaee M, Yoo H, Larson D T, Zhao S Y F, Taniguchi T, Watanabe K, Brower-Thomas T L, Kaxiras E and Kim P 2018 Heterointerface effects in the electrointercalation of van der Waals heterostructures *Nature* **558** 425–9

[30] Sood A *et al* 2018 An electrochemical thermal transistor *Nat. Commun.* **9** 4510

[31] Yalon E *et al* 2017 Energy dissipation in monolayer MoS_2 electronics *Nano Lett.* **17** 3429–33

[32] Zhang X, Sun D, Li Y, Lee G-H, Cui X, Chenet D, You Y, Heinz T F and Hone J C 2015 Measurement of lateral and interfacial thermal conductivity of single- and bilayer MoS_2 and MoSe2 using refined optothermal raman technique *ACS Appl. Mater. Interfaces* **7** 25923–9

[33] Yalon E *et al* 2017 Temperature-dependent thermal boundary conductance of monolayer MoS_2 by Raman thermometry *ACS Appl. Mater. Interfaces* **9** 43013–20

[34] Sood A, Xiong F, Chen S, Cheaito R, Lian F, Asheghi M, Cui Y, Donadio D, Goodson K E and Pop E 2019 Quasi-ballistic thermal transport across MoS_2 thin films *Nano Lett.* **19** 2434–42

[35] Wan J Y *et al* 2015 *In situ* investigations of Li-MoS_2 with planar batteries *Adv. Energy Mater.* **5** 1401742

[36] Wang H T, Lu Z Y, Kong D S, Sun J, Hymel T M and Cui Y 2014 Electrochemical tuning of MoS_2 nanoparticles on three-dimensional substrate for efficient hydrogen evolution *ACS Nano* **8** 4940–7

[37] Noerochim L, Yurwendra A O and Susanti D 2016 Effect of carbon coating on the electrochemical performance of LiFePO4/C as cathode materials for aqueous electrolyte lithium-ion battery *Ionics* **22** 341–6

[38] Li Z J, Peng Z Z, Zhang H, Hu T, Hu M M, Zhu K J and Wang X H 2016 [100]-Oriented LiFePO4 nanoflakes toward high rate Li-ion battery cathode *Nano Lett.* **16** 795–9

[39] Zhang S S 2013 Liquid electrolyte lithium/sulfur battery: fundamental chemistry, problems, and solutions *J. Power Sources* **231** 153–62

[40] Ngai K S, Ramesh S, Ramesh K and Juan J C 2016 A review of polymer electrolytes: fundamental, approaches and applications *Ionics* **22** 1259–79

[41] Xu H L, Fathipour S, Kinder E W, Seabaugh A C and Fullerton-Shirey S K 2015 Reconfigurable ion gating of 2H-$MoTe_2$ field-effect transistors using Poly(ethylene oxide)-$CsClO_4$ solid polymer electrolyte *ACS Nano* **9** 4900–10

[42] Ye J T, Zhang Y J, Akashi R, Bahramy M S, Arita R and Iwasa Y 2012 Superconducting dome in a gate-tuned band insulator *Science* **338** 1193–6

[43] Jo S, Costanzo D, Berger H and Morpurgo A F 2015 Electrostatically induced superconductivity at the surface of WS_2 *Nano Lett.* **15** 1197–202

[44] Lu J M, Zheliuk O, Leermakers I, Yuan N F Q, Zeitler U, Law K T and Ye J T 2015 Evidence for two-dimensional Ising superconductivity in gated MoS_2 *Science* **350** 1353–7

[45] Shin Y S *et al* 2020 Li intercalation effects on interface resistances of high-speed and low-power WSe_2 field-effect transistors *Adv. Funct. Mater.* **30** 2003688

[46] Gorinski N, Kowalsman N, Renner U, Wirth A, Reinartz M T, Seifert R, Zeug A, Ponimaskin E and Niv M Y 2012 Computational and experimental analysis of the transmembrane domain 4/5 dimerization interface of the serotonin 5-HT1A receptor *Mol. Pharmacol.* **82** 448–63

[47] Larson D T, Fampiou I, Kim G and Kaxiras E 2018 Lithium intercalation in graphene–MoS_2 heterostructures *J. Phys. Chem.* C **122** 24535–41

[48] Sharbati M T, Du Y, Li Y, Ardolino N, Liu P, Yun M and Xiong F 2018 Low-power, electrochemically-tunable graphene synapses for neuromorphic computing *Advanced Materials* **30** 1802353

[49] Zhu J *et al* 2018 Ion gated synaptic transistors based on 2D van der Waals crystals with tunable diffusive dynamics *Adv. Mater.* **30** 1800195

[50] Wan Q, Shao Q, Sharbati M T, Erickson J R, Wang K and Xiong F 2019 (Bi0.2Sb0.8)2Te3 based dynamic synapses

with programmable spatio-temporal dynamics *APL Materials* **7** 101107
[51] Zhu X, Li D, Liang X and Lu W D 2019 Ionic modulation and ionic coupling effects in MoS_2 devices for neuromorphic computing *Nat. Mater.* **18** 141–8
[52] Kiriya D, Tosun M, Zhao P D, Kang J S and Javey A 2014 Air-stable surface charge transfer doping of MoS_2 by benzyl viologen *J. Am. Chem. Soc.* **136** 7853–6
[53] Chakraborty B, Bera A, Muthu D V S, Bhowmick S, Waghmare U V and Sood A K 2012 Symmetry-dependent phonon renormalization in monolayer MoS_2 transistor *Phys. Rev.* B **85** 161403
[54] Lloyd D, Liu X, Christopher J W, Cantley L, Wadehra A, Kim B L, Goldberg B B, Swan A K and Bunch J S 2016 Band gap engineering with ultralarge biaxial strains in suspended monolayer MoS_2 *Nano Lett.* **16** 5836–41
[55] Hsieh W P, Lyons A S, Pop E, Keblinski P and Cahill D G 2011 Pressure tuning of the thermal conductance of weak interfaces *Phys. Rev.* B **84** 184107
[56] Nyby C *et al* 2020 Visualizing energy transfer at buried interfaces in layered materials using picosecond x-rays *Adv. Funct. Mater.* **30** 2002282
[57] Suryavanshi S V and Pop E 2016 S2DS: physics-based compact model for circuit simulation of two-dimensional semiconductor devices including non-idealities *J. Appl. Phys.* **120** 224503
[58] Monachon C, Weber L and Dames C 2016 Thermal boundary conductance: a materials science perspective *Annu. Rev. Mater. Res.* **46** 433–63
[59] Yue Y N, Zhang J C, Xie Y S, Chen W and Wang X W 2017 Energy coupling across low-dimensional contact interfaces at the atomic scale *Int. J. Heat Mass Transfer* **110** 827–44
[60] Sood A, Cho J, Hobart K D, Feygelson T I, Pate B B, Asheghi M, Cahill D G and Goodson K E 2016 Anisotropic and inhomogeneous thermal conduction in suspended thin-film polycrystalline diamond *J. Appl. Phys.* **119** 175103
[61] Eda G, Yamaguchi H, Voiry D, Fujita T, Chen M W and Chhowalla M 2011 Photoluminescence from chemically exfoliated MoS_2 *Nano Lett.* **11** 5111–6

Tuning Electrical and Interfacial Thermal Properties of Bilayer MoS_2 via Electrochemical Intercalation

Feng Xiong[1, *], Eilam Yalon[2,3], Connor J. McClellan[2], Jinsong Zhang[4], Ozgur B. Aslan[4,5], Aditya Sood[4], Jie Sun[4], Christopher Andolina[6], Wissam A. Saidi[6], Kenneth E. Goodson[7], Tony F. Heinz[5, 8], Yi Cui[4, 8], and Eric Pop[2, 4]

[1]*Department of Electrical and Computer Engineering, University of Pittsburgh, Pittsburgh, PA 15261, USA*

[2]*Department of Electrical Engineering, Stanford University, Stanford, CA 94305, USA*

[3]*Present address: Department of Electrical Engineering, Technion 32000, Israel*

[4]*Department of Materials Science and Engineering, Stanford University, Stanford, CA 94305, USA*

[5]*Department of Applied Physics, Stanford University, Stanford, CA 94305, USA*

[6]*Department of Mechanical Engineering and Materials Science, University of Pittsburgh, Pittsburgh, PA 15261, USA*

[7]*Department of Mechanical Engineering, Stanford University, Stanford, CA 94305, USA*

[8]*Stanford Institute for Materials and Energy Sciences, SLAC National Accelerator Laboratory, 2575 Sand Hill Road, Menlo Park, CA 94025, USA*

[*]E-mail: f.xiong@pitt.edu

Supporting Information

S1. Device fabrication

We fabricated our MoS_2 device through mechanical exfoliation, electron-beam lithography (EBL), and metal deposition. Our electrochemical cell consists of the MoS_2 flake (the working electrode), lithium iron phosphate (LFP as the reference electrode), and PEO electrolyte with $LiClO_4$. We wire-bonded electrodes to Cu tapes for electrochemical measurements. Figure S1a shows an optical image of a typical device and Fig. S1b shows the in-situ Raman set up.

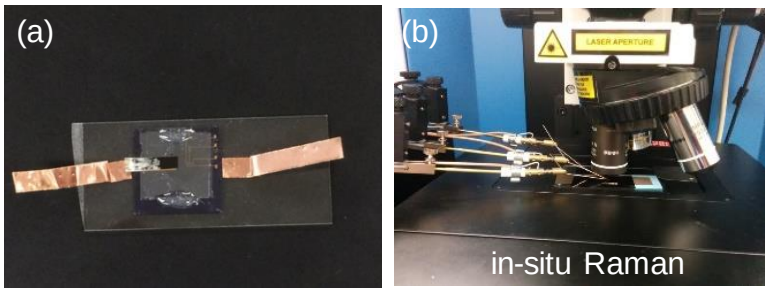

Figure S1: Electrochemical device and in-situ Raman set up. (a) Optical image of a packaged electrochemical MoS_2 device with LFP electrode and PEO electrolyte. (b) Set up for in-situ Raman measurements while we perform Li intercalation, showing probe arms on the left.

S2. Temperature dependence of electrical resistance

We measured the electrical resistance of pristine and lithiated MoS_2 as a function of temperature (cooling from 330 K to 1.6 K), as shown in Fig. S2. We observed over 100× decrease in resistance at all temperatures, between MoS_2 and $Li_{1.0}MoS_2$, upon Li intercalation.

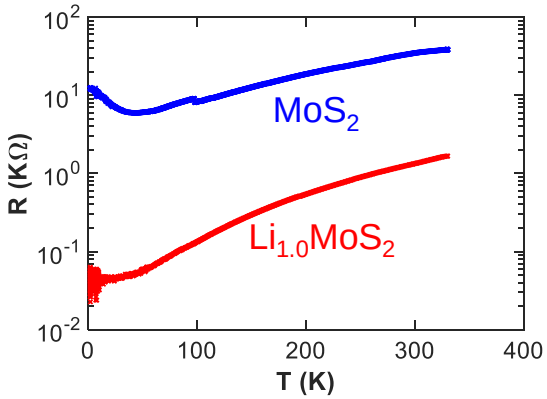

Figure S2: Temperature dependence of electrical resistance of MoS_2 and $Li_{1.0}MoS_2$.

S3. Laser spot calibration

We performed the knife edge experiments [1-3] (Fig. S3a) to characterize our laser spot size. We scanned the laser along the MoS_2 flake across a sharp edge of a gold metal film, which blocks the Raman signal. We then extracted the laser spot size (r_0) by fitting an error function to the measured profile (Fig. S3b). We also repeated the knife edge measurement after applying the PEO

electrolyte (Fig. S3c). The spot radius without and with PEO are r_0 = 310 ± 30 nm and 370 ± 33 nm, respectively.

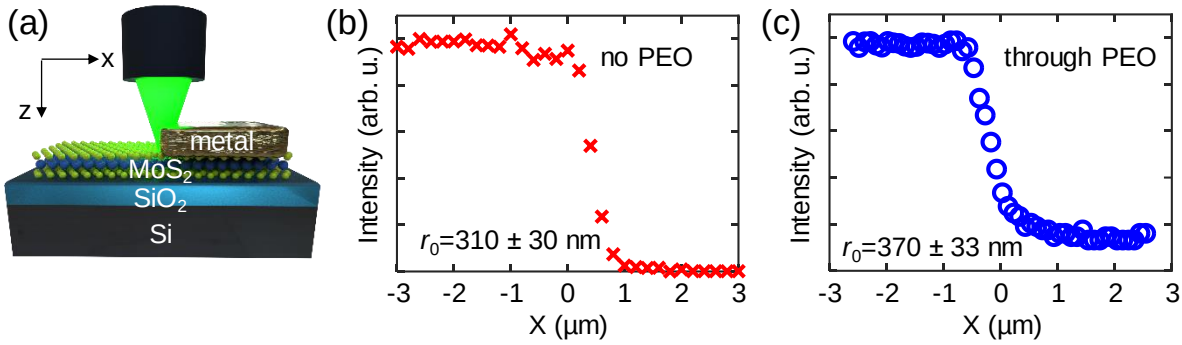

Figure S3: Laser (532 nm) spot size. (**a**) Schematics of the knife edge measurements for determining laser spot size. The measured intensity and the error function fit versus the location along the horizontal axis without (**b**) and with (**c**) the PEO electrolyte. The spot radius without and with PEO are r_0 = 310 ± 30 nm and 370 ± 33 nm, respectively.

S4. Sensitivity of laser heating to thermal conductivity of MoS_2

Through finite element simulations (Fig. S4), we illustrate that the heating of our MoS_2 devices on 90-nm SiO_2/Si substrate are insensitive to the in-plane thermal conductivity of MoS_2, within any realistic variations. This suggests that our Raman thermometry measurements with spot sizes > 300 nm, are only sensitive to the thermal boundary conductance (TBC) at the interface between MoS_2 and the supporting SiO_2 substrate.

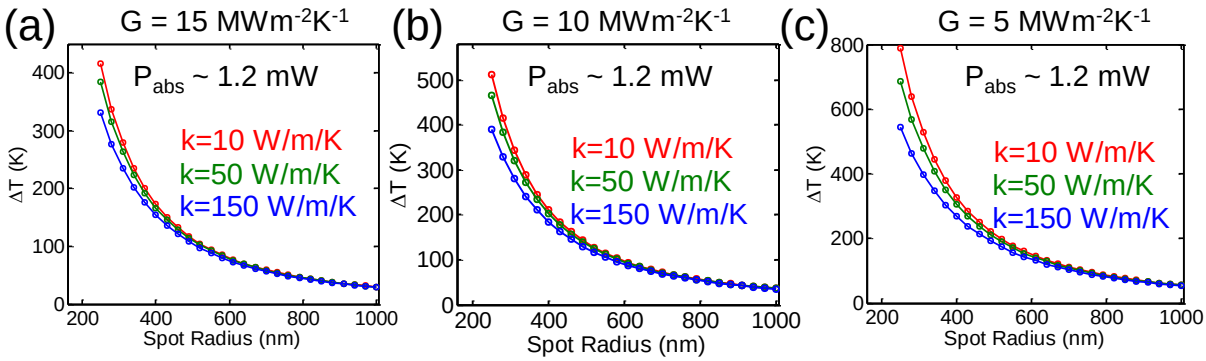

Figure S4: Lack of sensitivity to the in-plane thermal conductivity of MoS_2. Simulated temperature rises in MoS_2 with different values of TBCs, G = **(a)** 15 **(b)** 10 and **(c)** 5 $MWm^{-2}K^{-1}$. The in-plane thermal conductivities of MoS_2 were varied to three different values: 10 (red), 50 (green), and 150 (blue) $Wm^{-1}K^{-1}$.

S5. Temperature-dependent Raman peak shifts

We performed temperature-dependent calibrations of Raman peaks (A_{1g} and E^1_{2g} modes) for bilayer (2L) pristine MoS_2 and lithiated Li_xMoS_2 at different Li concentrations (x = 0.1, 0.2, 0.4, 0.8, and 1.0). As shown in Fig. S5, we fit a linear relationship between the Raman peak position ω and the sample temperature T: $\omega(T) = \omega_0 + \chi(T - T_0)$, where ω_0 is the peak position at room temperature T_0 and χ is the temperature dependence coefficient for the particular Raman mode. The χ ranged from -0.013 to -0.015 $cm^{-1}/$ ℃. We kept the temperature of the Li_xMoS_2 sample below 100 ℃ during the calibrations to avoid unintentional phase transformation (1T to 2H) and to minimize ionic diffusion (and therefore a change in carrier concentration) that has been observed at high temperature annealing (> 300 ℃) in chemically lithiated MoS_2 thin films [4, 5].

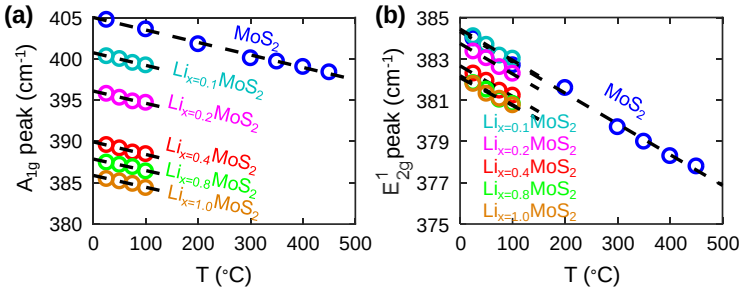

Figure S5: Raman temperature dependence calibration. Temperature calibrations of both pristine and lithiated bilayer MoS_2 for **(a)** A_{1g} and **(b)** E^1_{2g} modes. **(a)** For A_{1g} modes, the temperature coefficients χ = 0.015, 0.015, 0.015, 0.014, 0.014 $cm^{-1}/$ ℃ for x = 0, 0.1, 0.2, 0.4, 0.8, and 1.0 (Li_xMoS_2) respectively. **(b)** For E^1_{2g} modes, the temperature coefficients χ = 0.015, 0.015, 0.015, 0.014, 0.013 $cm^{-1}/$ ℃ for x = 0, 0.1, 0.2, 0.4, 0.8, and 1.0 (Li_xMoS_2) respectively.

S6. MoS_2 absorption

We measured the absorption of monolayer MoS_2 at different wavelengths (Fig. S6a).[3] The optical dielectric function of MoS_2 is governed by the direct transitions (A, B excitons etc.) [6], which have comparable peak energies and line widths for monolayer and bilayers [7]. Furthermore, the oscillator strengths of those transitions are conserved even up to the bulk limit [6]. Thus, we expect the optical dielectric functions of monolayer and bilayer MoS_2 to be very similar away from the peak energies of those transitions, such as at a wavelength of 532 nm. Thus, we expect that the absorption of bilayer MoS_2 is twice of that of the monolayer, as it is proportional to the material thickness in this regime [8]. As the temperature dependence of the absorption at 532 nm arises from the broadening of the C feature, we also expect a similar trend for both thicknesses with increasing temperature away from the peak energies. The temperature dependence of absorption

at selected wavelengths for the monolayer is illustrated in Fig. S6b. The absorption of few-layer lithiated MoS_2 (4 nm thick) is calculated from the transmission contrast shown in Fig. S6c [9]. The enhancement factors from the SiO_2/Si substrate are listed in Table S1.

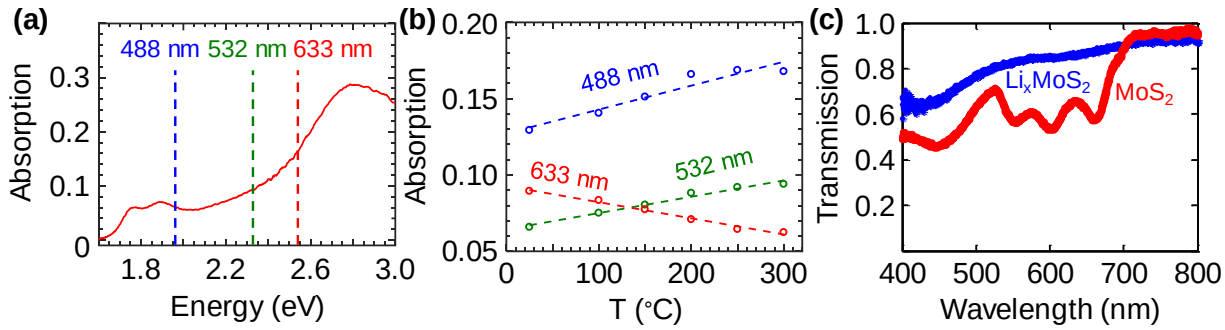

Figure S6: Absorption coefficient of MoS_2. (a) Measured absorption coefficient of free-standing monolayer MoS_2 across the spectrum.[3] We used a laser with a wavelength of 532 nm in our Raman measurements. (b) Temperature dependence of the absorption coefficients of monolayer MoS_2 at selected wavelengths.[3] (c) Transmission coefficient of pristine and lithiated 6-7 layer (4 nm thick) MoS_2 [9].

Device Configuration	**Intensity Enhancement @ 488 nm**	**Intensity Enhancement @ 532 nm**	**Intensity Enhancement @ 633 nm**
90 nm SiO_2/Si	1.768	1.745	1.527
25 µm PEO + 90 nm SiO2/Si	1.476	1.461	1.323

Table S1: Enhancement factor for absorption on 90 nm SiO_2/Si substrates with and without the top PEO layer at several wavelengths.

S7. Thermal modeling

A 3D numerical thermal model [10] is employed to calculate the temperature rise in MoS_2 due to the absorbed laser power. A transfer-matrix approach is adopted for the multilayer geometry (electrolyte-MoS_2-SiO_2-Si), that takes into account radial heat-spreading effects, Gaussian heat flux input by the laser, bidirectional heat flow (i.e. upwards into the electrolyte, and downwards into the substrate), and finite thermal boundary conductance at the interfaces [10]. The thermal conductivities for PEO electrolyte, bilayer MoS_2, SiO_2, and highly-doped Si are assumed at 0.2,

50, 1.4, and 100 $Wm^{-1}K^{-1}$, respective. The TBC for the PEO-MoS_2 interface is assumed at 80 $MWm^{-2}K^{-1}$. With a given input power and temperature rise, the MoS_2-SiO_2 TBC is the only fitting parameter we need to solve.

We also model the laser heating using a finite element thermal simulation (COMSOL Multiphysics ®) to supplement our numerical thermal model. The Fourier heat diffusion equation is solved with cylindrical coordinates (2D axisymmetric configuration) and a Gaussian shaped beam heat source following the procedure outlined in Ref. [3]. The bottom of the Si substrate (500 μm thick) is held at ambient temperature (isothermal boundary condition) and other surface boundaries are thermally insulating (adiabatic boundary condition). The thermal properties of the SiO_2 and Si substrate are well known, including their temperature dependence around room temperature (values are listed in Ref. [3]). The heat is dissipated mostly in the cross-plane direction into the Si substrate, typical for supported films as discussed in the main text. We therefore set k = 50 $Wm^{-1}K^{-1}$ for the in-plane thermal conductivity of MoS_2 in our thermal model and validated that the extracted TBC values were insensitive (within measurement uncertainty) to any realistic variations of k. Given these inputs to the finite element thermal model, the MoS_2-SiO_2 TBC remains a single fitting parameter.

S8. Density functional theory calculations

To correlate with experimental results, we carried out first-principles density functional theory (DFT) calculations to study the vibrational modes of the Li_xMoS_2 systems. We use the Perdew-Burke-Ernzerhof (PBE) exchange-correlational functional [11] within the Vienna *Ab initio* Simulation Package(VASP) [12, 13], and projector-augmented wave potentials using a planewave cutoff energy of 500 eV. The phonon calculations are carried out using Phonopy [14] with the finite displacement method [14]. To model experimental observed Li^+ induced shifts on the of A^1_g and E^1_{2g} Raman frequencies in the 2H-MoS_2 lattice, we carried simulations on 2x2x1 MoS2 supercell and included 1-4 Li atoms between the two layers. For each Li concentration, we determined the most stable intercalation configuration, as seen in the inset of Figure S7. The Raman A^1_g and E^1_{2g} bands in the pristine MoS_2 structure are readily identified by atomic motions (see insets of Figure S7). The A^1_g band is identified by the static position of the Mo atoms and the opposing motion of each bound S atom along the *z*-axis. Whereas the E^1_{2g} band is described by the opposing parallel

motions of Mo and both bound S atoms along the *x* and/or *y* planes. It should be noted that identification of the Raman modes upon addition of Li into our MoS_2 model becomes more ambiguous as the Li atoms disrupt the unit cell symmetry, participate in parallel vibrations with Mo and S atoms, and/or dampen vibrations of nearby atoms. These observed disruptions are common when pristine systems acquire defects such as intercalated Li [15]. In our study, we find that the identification of the Raman A^1_g bands in Li_xMoS_2 where x = 0.25, 0.5, and 0.75 were found to be especially ambiguous because of the supercell symmetry breaking of the intercalated Li atoms. Therefore, we averaged similar vibrational modes that have A^1_g band character. Overall, we show good agreement between our DFT based calculations and the experimental Raman shifts (Figure 3b-c) and are similar to Raman shifts observed in Li_xMoS_2 powdered systems [16]. For the A^1_g band, we note an initial increase in frequencies at x = 0.25 followed by a decrease as concentration Li increases which is not observed in the experiment results. The predicted lower energy and wider apparent shift in both Raman bands A^1_g and E^1_{2g} (5.3 and 12.7 cm^{-1}, respectively) are a result of experimental parameters that were not modeled in our DFT calculations such as experimental temperature/ambient conditions and SiO_2 support/overall sample thickness.

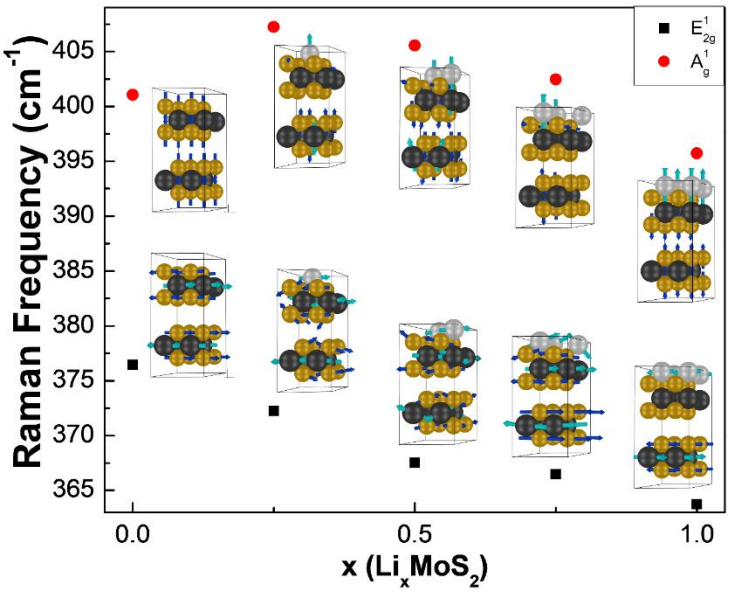

Figure S7: DFT based calculations. The VASP-Phonopy calculated shift in the A^1_g and E^1_{2g} Raman bands as a function of intercalated Li^+. Inset figures show representative lattice vibrations that correspond to the A^1_g and E^1_{2g} Raman bands.

Supporting Information References:

[1] Cai W, Moore A L, Zhu Y, Li X, Chen S, Shi L and Ruoff R S 2010 Thermal transport in suspended and supported monolayer graphene grown by chemical vapor deposition *Nano Lett.* **10** 1645-51

[2] Mauck M 1979 Knife-edge profiling of Q-switched Nd: YAG laser beam and waist *Applied optics* **18** 599-600

[3] Yalon E, Aslan Ö B, Smithe K K H, McClellan C J, Suryavanshi S V, Xiong F, Sood A, Neumann C M, Xu X, Goodson K E, Heinz T F and Pop E 2017 Temperature-Dependent Thermal Boundary Conductance of Monolayer MoS2 by Raman Thermometry *Acs Appl Mater Inter* **9** 43013-20

[4] Eda G, Yamaguchi H, Voiry D, Fujita T, Chen M W and Chhowalla M 2011 Photoluminescence from Chemically Exfoliated MoS_2 *Nano Lett* **11** 5111-6

[5] Kappera R, Voiry D, Yalcin S E, Branch B, Gupta G, Mohite A D and Chhowalla M 2014 Phase-engineered low-resistance contacts for ultrathin MoS_2 transistors *Nat Mater* **13** 1128-34

[6] Li Y, Chernikov A, Zhang X, Rigosi A, Hill H M, van der Zande A M, Chenet D A, Shih E-M, Hone J and Heinz T F 2014 Measurement of the optical dielectric function of monolayer transition-metal dichalcogenides: MoS_2, $MoSe_2$, WS_2, and WSe_2 *Phys. Rev. B* **90** 205422

[7] Mak K F, Lee C, Hone J, Shan J and Heinz T F 2010 Atomically Thin MoS_2: A New Direct-Gap Semiconductor *Phys. Rev. Lett.* **105** 136805

[8] Yilei L and Tony F H 2018 Two-dimensional models for the optical response of thin films *2D Materials* **5** 025021

[9] Xiong F, Wang H T, Liu X G, Sun J, Brongersma M, Pop E and Cui Y 2015 Li Intercalation in MoS_2: In Situ Observation of Its Dynamics and Tuning Optical and Electrical Properties *Nano Lett* **15** 6777-84

[10] Sood A, Cho J, Hobart K D, Feygelson T I, Pate B B, Asheghi M, Cahill D G and Goodson K E 2016 Anisotropic and inhomogeneous thermal conduction in suspended thin-film polycrystalline diamond *J Appl Phys* **119** 175103

[11] John P. Perdew K B, Matthias Ernzerhof 1996 Generalized Gradient Approximation Made Simple *Phys. Rev. Lett.* **77** 4

[12] G. Kresse J F 1996 Efficient iterative schemes for ab initio total-energy calculations using a plane-wave basis set *Phys. Rew.* **54** 11168

[13] Shishkin M, Marsman M and Kresse G 2007 Accurate quasiparticle spectra from self-consistent GW calculations with vertex corrections *Phys. Rev. Lett.* **99** 246403

[14] Togo A and Tanaka I 2015 First principles phonon calculations in materials science *Scripta Mater.* **108** 1-5

[15] Saidi W A 2014 Effects of Topological Defects and Diatom Vacancies on Characteristic Vibration Modes and Raman Intensities of Zigzag Single-Walled Carbon Nanotubes *J. Phys. Chem. A* **118** 7235-41

[16] Xia J, Wang J, Chao D, Chen Z, Liu Z, Kuo J-L, Yan J and Shen Z X 2017 Phase evolution of lithium intercalation dynamics in 2H-MoS 2 *Nanoscale* **9** 7533-40